A New Neural-network-based Model
for Localizing Synthetic Aperture Radar Images

Guoshi Liu,[1] Keyu Li,[2] Xin Liu,[2*] Yingfei Gao,[3] and Hui Li[1]

[1]School of Civil Architectural Engineering, Shaoyang University, Shaoyang 422000, China
[2]School of Automation and Electronic Information, Xiangtan University, Xiangtan 411105, China
[3]Shaoyang City Planning and Design Institute, Shaoyang 422000, China

The geometric processing of spaceborne synthetic aperture radar (SAR) images plays a crucial role in achieving the high-precision positioning of SAR images. Traditional SAR image geometric processing models include rigorous sensor models and rational polynomial coefficient models. However, these models are not always fully applicable to complex SAR image geometric processing scenarios. To address this issue, we propose an innovative framework for spaceborne SAR image geometric processing, aiming to realize the training of SAR image geometric processing models. The framework primarily relies on the generation of coordinate samples based on the rigorous imaging model of spaceborne SAR and utilizes a network model called the Spaceborne Synthetic Aperture Radar Coordinates Points-Radial Basis Function Neural Network (SARCoorP-RBFNet), composed of radial basis function neurons, to approximate the mapping relationship between the heterogeneous spatial coordinates and the corresponding ground coordinates. The network is trained using the generalized inverse matrix method to achieve more stable performance. The proposed method has been tested on spaceborne SAR images covering most cities in China with resolutions of 1, 3, 5, 8, and 25 m in the imaging area. The results demonstrate that SARCoorP-RBFNet achieves a large number of well-fitted heterogeneous spatial coordinate point pairs with an accuracy higher than 5% of a pixel and exhibits significant advantages in complex scenarios involving the geometric processing of multiple images.

1. Introduction

Synthetic aperture radar (SAR) technology has been widely used in military and civilian fields owing to its ability to observe Earth in all-weather, all-day, multi-dimensional, and high-resolution imaging. It has become one of the most important tools for Earth observation. With the advancement of space SAR technology, SAR image geometry positioning technology is developing rapidly. The preprocessing stage of SAR image geometry positioning technology involves the creation of SAR geometry imaging models. Currently, there are two main SAR

geometry imaging models: Range Doppler (RD)[1] and Rational Polynomial Coefficient (RPC).[2] The RD model can provide high-precision data but is severely dependent on physical sensor parameters,[2–4] limiting its application. The RPC model can fit SAR images under ideal zero Doppler conditions and can replace the RD model.[4] However, previous studies have shown that the RPC model has confidentiality issues because it can easily calculate the attitude information of remote sensing satellites.[5,6]

In recent years, with the continuous development of neural networks, the numerical fitting method based on neural networks has rapidly advanced. Neural networks have a hierarchical structure of data characteristics, which can represent high complexity functions,[7] providing a theoretical basis for the neural network model to fit the RD model. Compared with traditional numerical fitting methods, the neural network approach has the advantage of adapting to different data and performing a complete analysis of multiple variables.[8,9] Currently, there is extensive research on neural-network-based remote sensing image classification, object detection, and other related areas. However, there is relatively limited research on SAR image geometric processing. One of the challenges facing the geometric processing of SAR images is the lack of intelligent fitting models suitable for complex scenarios. Existing models are primarily designed for the geometric processing of single-scene SAR images, and their applicability is limited, thus unable to support the geometric processing of multiple SAR images in complex scenarios.

Therefore, we would like to adopt the neural network approach for the geometric processing of SAR images. However, neural networks rely on data-driven learning, and currently, there are no publicly available datasets that can support the training of neural networks specifically for SAR image geometric processing.

In this paper, we present a targeted network fitting model for the geometric processing of satellite-borne SAR image formation, which takes into full consideration the data characteristics of satellite-borne SAR images. On the basis of the rigorous geometric model of satellite-borne SAR imaging, heterogeneous spatial coordinate point pairs are generated. A targeted network fitting model is designed specifically for SAR image formation patterns and imaging coverage areas. The radial basis network is utilized to fit the mapping relationship between different spatial coordinate point pairs.

The main contributions of this paper can be summarized into the following two aspects:

1) We propose a network fitting model for the geometric processing of satellite-borne SAR image formation, referred to as Spaceborne Synthetic Aperture Radar Coordinates Points-Radial Basis Function Neural Network (SARCoorP-RBFNet). We utilize the RD model to generate training samples and employ radial basis function (RBF) networks as the foundational structure for fitting the coordinate point pairs.

2) We conduct targeted experiments and thoroughly validate our approach using SAR images with resolutions of 1, 3, 5, 8, and 25 m, covering multiple cities in China. The experimental results demonstrate the effectiveness of our method in fitting the mapping relationship between coordinate point pairs from different spatial locations for imaging geometric processing, while achieving reliable accuracy.

2.   Related Work

The purpose of SAR image geometric processing is to enhance the geometric positioning accuracy of SAR images. Currently, the mainstream geometric processing models primarily rely on improvements based on the RD and RPC models.

Back in 1981, Brown introduced a method for the absolute positioning of individual pixels in SAR images without the need for ground control points.[10] This approach relied on remote sensing ephemeris data and the characteristic parameters of the SAR data acquisition system as inputs. In 1993, Bamler and Schättler presented a paper on SAR image geocoding, where he parameterized the orbit model, range equation, and Doppler frequency equation using polynomials.[11] He established an RD model using the model parameters extracted from radar processing parameters, enabling indirect resampling and positioning. Iterative methods were employed for the spatial solution between the geographic and image coordinates. On the other hand, the RPC model has long been widely used in optical satellite remote sensing data processing. It was not until 2010 when Vassilaki and Ioannidis first applied RPC to high-resolution SAR imagery, conducting target localization experiments using TerraSAR images with a model replacement accuracy of five pixels.[12] Eftekhari *et al.* presented a method for solving the RPC model, which was based on sensor parameter calibration.[13] Subsequently, as the RPC model matured, Capaldo *et al.* conducted research on stereo positioning algorithms and regional network adjustment methods based on the RPC model.[14] Sekhar *et al.* proposed an RPC model based on the orthorectification of SAR images.[15]

We can observe that both the RD and RPC models are solely employed for the geometric processing of single-scene imagery. Consequently, to some extent, they lack general applicability when confronted with scenarios involving the geometric processing of multiple SAR images.

In recent years, with the continuous development of neural network technology, foreign researchers have increasingly recognized its application in the field of remote sensing. For example, Furukawa applied convolutional neural networks to the study of motion invariance in SAR imaging.[16] Mason *et al.* proposed a cyclic autoencoder network structure based on the iterative shrinkage-thresholding algorithm, which was combined with SAR modeling to form focused images in the presence of phase uncertainty.[17] Anantrasirichai *et al.* and Valade *et al.* utilized convolutional neural networks to determine whether a single SAR interferometer includes deformation.[18,19] Moreover, Gaddes *et al.* conducted multiple studies using blind signal separation methods to identify signs of instability in interferometric time series and utilized convolutional neural networks to locate deformations in the interferograms.[20,21] Note that, so far, the application of neural networks in SAR geometric positioning has not been proposed. Therefore, a neural network fitting method for the geometric processing of satellite-borne SAR images is still lacking.

3.   Materials and Methods

In response to the demand for the high-precision fitting of coordinate points in SAR image geometric processing, we propose a targeted network fitting model inspired by the research

advancements in the universal approximation theory of neural networks. As illustrated in Fig. 1, our approach comprises the folloowing two modules:

1) Dataset construction module: We generate coordinate point samples based on the rigorous geometric model of satellite-borne SAR imaging.
2) Coordinate fitting module: We design a network for fitting the SAR image geometric processing, enabling the learning of mapping relationships between different spatial points.

3.1 Dataset construction module

The training of neural network models for SAR image geometric processing requires coordinate point pairs from different scenarios. Currently, there is a lack of benchmark datasets for neural network learning in SAR image geometric processing. To address the issue of insufficient training data, a distance-Doppler model is used to generate coordinate point samples.

Establishing a SAR image geometric processing model is the basis for photogrammetric positioning processing. The SAR image geometric processing model describes the mathematical relationship between the geodetic coordinates of ground points and their corresponding image coordinates.[22] On the basis of this mathematical relationship between the pixel points of the image and the ground point coordinates, the RD model can be constructed, which includes the ellipsoid, oblique distance, and Doppler equations.[23–25] The ellipsoid equation is

$$\frac{\left(X^2 + Y^2\right)}{\left(a_e + h\right)^2} + \frac{Z^2}{B^2} = 1, \tag{1}$$

where $R_{AO} = (X, Y, Z)^T$ denotes the position vector of the ground target point, a_e and B are the long and short semi-axes of the WGS84 Earth ellipsoid, respectively, and h is the ellipsoidal height of the target point.
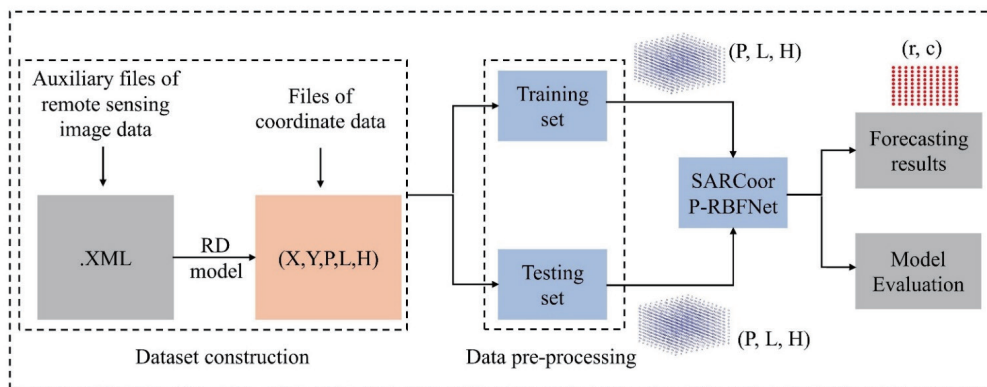

Fig. 1. (Color online) Model of proposed SARCoorP-RBFNet algorithm.

The oblique distance equation is

$$R^2 = (X - X_S)^2 + (Y - Y_S)^2 + (Z - Z_S)^2, \tag{2}$$

where R is the distance between the SAR satellite and the ground point and $R_{SO} = (X_S, Y_S, Z_S)^T$ denotes the position vector of the satellite.

The Doppler equation is

$$f_D = -\frac{2}{\lambda R}(R_{SO} - R_{AO}) \times (V_{SO} - V_{AO}), \tag{3}$$

where f_D is the Doppler center frequency of the ground target, and R_{SO} and V_{SO} are the position and velocity vectors of the satellite at the imaging time of the ground target point, respectively. R_{AO} is the position vector of the target point, V_{AO} is the velocity vector of the target point, and λ is the radar wavelength.

We can use the formula above to determine the functional relationship between a ground object's coordinate location in the WGS-84 coordinate system and its equivalent image space coordinate position.

3.2   SARCoorP-RBFNet architecture

Neural networks can be divided into global and local approximation networks. Any output of the global approximation network is affected by the threshold and weight of the neural network node. The output of the local approximation network is only affected by the connection weight between several local nodes of the network input. Therefore, local approximation networks have a higher learning speed than global ones.[26] The RBF neural network is a three-layer forward local approximation network; the RBF is embodied in the fact that it can approximate any nonlinear function with arbitrary accuracy, which is based on the well-known Stone–Weierstrass theorem and other related theoretical foundations. The RBF neural network can effectively bypass the system complexity and has strong adaptability to new samples. The mapping relationship between the object and image point coordinates of spaceborne SAR images has nonlinear characteristics. Therefore, it is feasible to select the RBF neural network for modeling to fit this nonlinear mapping relationship.

The RBF neural network is a linear combination of a set of weighted RBFs in the mathematical sense, generally composed of input, hidden, and output layers. The transformation from the input space to the hidden layer space is nonlinear, whereas that from the hidden layer space to the output layer space is linear. The role of the hidden layer is to map vectors from dimension m to dimension n, so that the case of linear indivisibility in dimension m becomes linearly divisible in dimension n. In effect, it is the idea of a kernel function. For regression problems, it can be used to directly fit an unknown function.[27] The purpose of RBF neural network modeling is to determine that $f(x)$ makes $f(x^p) = y^p$ and $\forall p = 1, ..., D$, x^p is the input

vector (including latitude, longitude, and elevation information). The dimension D depends on the number of input samples, and the y^p term is the output parameter. Therefore, the RBF neural network attempts to map each input data $x^p = \left[x_i^p : 1, 2, ..., N \right]$ to its corresponding target value y^p.[28] Its topological network structure is shown in Fig. 2.

Considering the data characteristics of spaceborne SAR image geometric processing, the input of the network consists of pairs of geodetic coordinate points, while the output corresponds to pairs of image space coordinate points. Prior to feeding the data into the network for training, the samples should be normalized to the range (0, 1), as indicated by

$$y = \frac{\left(y_{max} - y_{min} \right) \times \left(x - x_{min} \right)}{\left(x_{max} - x_{min} \right)} + y_{min}. \tag{4}$$

The SARCoorP-RBFNet model incorporates Gaussian functions as RBFs. The model includes three important hyperparameters, namely, the number of nodes in the hidden layer, the width parameter of the RBF, and the weight of the output layer. The number of hidden layer nodes has an important impact on the performance of the RBF neural network. Too few nodes may result in an underfitted model, whereas too many may result in overfitting. In this study, we set the number of hidden layer nodes of 150 neurons. The width parameter determines the shape and size of the RBF; a larger width parameter results in a function that is flat and insensitive to the details of the input, whereas a smaller width parameter results in a function that is sharper and more sensitive to the details of the input. Therefore, we set the diffusion scalar that controls the width of the RBF to 0.1. The weight of the output layer reflects the degree of contribution of each hidden layer node to the final output, and we used the inverse hyperbolic function as the activation function to adjust the weight size. Specifically, this approach employs a method based on the clustering of the sample set, using the negative mean distance of the sample set as the threshold, to automatically calculate the activation function threshold. The network is trained using the generalized inverse matrix method to achieve more stable performance. For the prediction of new samples, the sim function is utilized, with the image space coordinate point
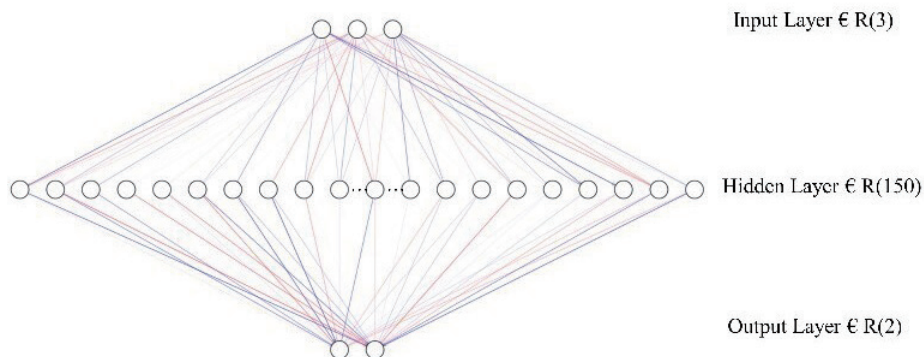

Fig. 2.   (Color online) Radial basis function (RBF) neural network topology graph: $R(x)$ denotes the number of neurons in the current layer.

pairs generated by the RD model serving as ground truth and the predicted image space coordinate points from the network model serving as test values. The root mean square error function is employed as the evaluation metric for assessing the error between the ground truth and the test values.

3.3   Experimental datasets

In this study, five imaging modes of GF-3 image standard view products were selected as test data, namely, Spot-Light (SL), Ultra-Fine-Strip (UFS), Fine-Strip-I (FSI), Quad-Polarised-Strip-I (QPSI), and Quad-Polarised-Strip-II (QPSII), covering areas such as Fangshan in Beijing (Northern China), Pudong in Shanghai (Eastern China), and Chengdu in Sichuan (Southwestern China). The study area is shown in Fig. 3. The detailed information of GF-3 satellite images is presented in Table 1.

3.4   Implementation details

To evaluate the proposed spaceborne SAR image geometric processing model, SARCoorP-RBFNet, in various imaging scenarios of spaceborne SAR imagery, this study applies SARCoorP-RBFNet to the assessment of GF-3 satellite image meta-products data. The experiments are conducted with a focus on two main aspects as follows.
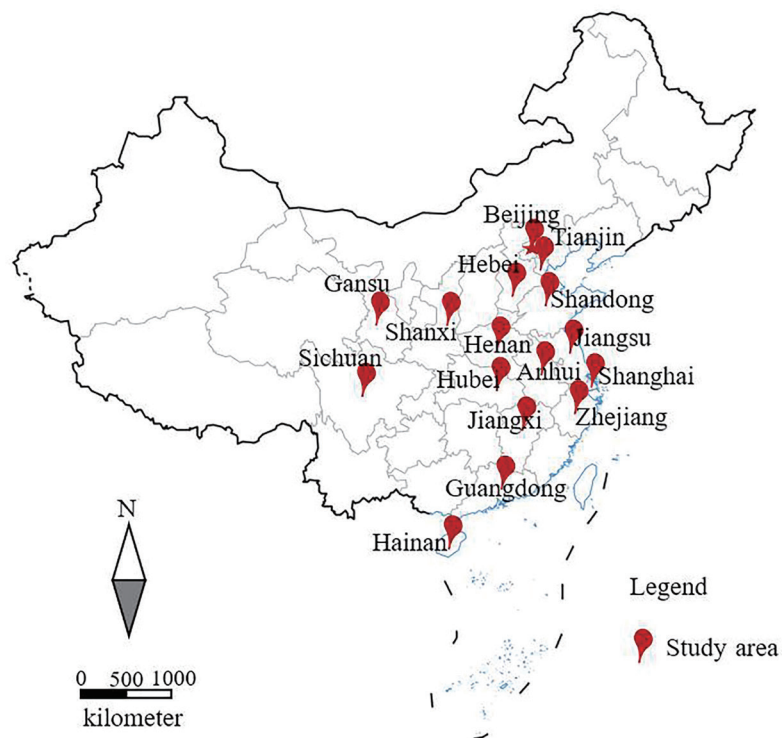

Fig. 3.   (Color online) Distribution of experimental data regions.

Table 1
GF-3 data information of study area.

Imaging mode	Image ID	Imaging date	Image width and height	Image width space and height space (m)	Imaging region	Latitude and longitude of image center
SL (1 m resolution)	SP_9563	23 March 2018	11666/ 34858	0.562111/0.312365	Shanghai Pudong	121.318072/31.194363
UFS (3 m resolution)	SP_1726	09 July 2018	16374/ 21955	1.124222/1.738304	Shanghai Pudong	121.204101/31.12610
	BF_4747	11 December 2019	16374/ 22383	1.124222/1.728993	Beijing Fangshan	115.996666/39.77400
FSI (5 m resolution)	SP_6958	02 August 2020	13182/ 21896	2.248443/2.611574	Shanghai Pudong	121.604695/31.13054
	BF_6710	22 August 2017	12875/ 21893	2.248443/2.608578	Beijing Fangshan	116.270416/39.82781
QPSI (8 m resolution)	SP_1557	05 July 2017	6907/7591	2.248443/4.754298	Shanghai Pudong	121.169319/31.26967
	BF_3116	19 January 2019	6014/7689	2.248443/5.361792	Beijing Fangshan	116.461109/39.81046
	AH_2710	19 January 2017	6675/11088	2.248443/4.670904	Anhui Hefei	117.143434/31.843186
	HZ_8163	01 April 2017	7898/6804	2.248443/5.199595	Henan Zhengzhou	113.168304/34.459211
	ZJ_2026	12 October 2017	6523/5983	2.248443/4.719058	Zhejiang	121.546764/29.910523
	SD_9870	17 January 2018	7209/7827	2.248443/4.818387	Shandong	121.438526/37.601950
	SW_4921	23 January 2018	6348/5986	2.248443/4.711925	Shanxi Weinan	109.057909/34.638829
	HW_7132	09 October 2018	8062/6810	2.248443/5.204732	Hainan Wenchang	110.545403/19.961587
	TJ_1776	19 October 2018	8062/6198	2.248443/5.540001	Tianjin	117.515814/39.244607
	GS_0981	22 October 2018	8062/7900	2.248443/5.283754	Gansu	100.357916/38.951206
	JX_9884	28 December 2018	8062/7480	2.248443/5.118558	Jiangxi	114.756659/25.680564
	BF_9197	21 December 2018	6014/7682	2.248443/5.366279	Beijing Fangshan	116.430612/40.003701
	HW_2194	11 December 2018	8062/6194	2.248443/5.548881	Hubei Wuhan	114.383576/30.499307
	GZ_1362	23 March 2021	7139/8869	2.248443/4.839266	Guangdong Zhanjiang	110.537795/21.122401
	SC_4783	16 May 2019	8062/6220	2.248443/5.530645	Sichuan Chengdu	103.257031/30.335912
	HX_4208	23 April 2017	5974/5254	2.248443/5.042253	Hebei Xingtai	114.556551/37.007159
	JN_5002	09 December 2017	5730/7684	2.248443/5.368656	Jiangsu Nanjing	118.500197/32.013715
QPSII (25 m resolution)	SP_3580	29 January 2017	9090/8974	2.248443/5.285367	Shanghai Pudong	121.624447/31.10519

SP: Shanghai Pudong; BF: Beijing Fangshan; SC: Sichuan Chengdu; HX: Hebei Xingtai; JN: Jiangsu Nanjing; GZ: Guangdong Zhanjiang; HW: Hubei Wuhan; JX: Jiangxi; GS: Gansu; TJ: Tianjin; HW: Hainan Wenchang; SW: Shanxi Weinan; SD: Shandong; ZJ: Zhejiang; HZ: Henan Zhengzhou; AH: Anhui Hefei.

(1) Evaluation of the fitting accuracy of the SARCoorP-RBFNet model trained on a single image. We used the coordinates of a single target point as an experimental sample to assess the fitting accuracy of the SARCoorP-RBFNet model in coordinate point data from two perspectives: images with different resolutions in the same region and images with the same resolution in different regions. To this end, we selected Shanghai's Pudong as a representative, which includes the images taken in the same region with different imaging modes (SL, UFS, FSI, QPSI, and QPSII). We selected the QPSI imaging mode, which includes images from Pudong, Fangshan, Chengdu, Xingtai, and Nanjing with the same resolution but different locations. To test the applicability of the SARCoorP-RBFNet model in SAR images with different resolutions and terrains, we conducted experiments on the coordinate point datasets of each image.

(2) On the basis of multi-image training, the fitting accuracy of the SARCoorP-RBFNet model was evaluated. To further assess the effectiveness of the proposed strategy, extensive experiments were conducted from the perspective of mixed training of multi-scene images. It should be emphasized that, in the sample preparation stage, k-means clustering technology was used to create matching labels for each scene image coordinate point data, which were used as inputs to the network along with latitude and longitude coordinates. Moreover, two

aspects were studied: the mixed training of different mode images in the same area and the mixed training of the same mode images in different areas. Specifically, SL, UFS, FSI, QPSI, and QPSII were selected as the five imaging modes for the mixed training of different modes in the Shanghai area. For the mixed training of the same mode images in different areas, the QPSI imaging mode was chosen, covering images of 16 regions in China.

4. Results

4.1 Evaluation of SARCoorP-RBFNet model's accuracy of fitting based on a single image training

Figure 4 shows the distribution of the fitting results of the SAR-CoorP-RBFNet model under different resolutions in the Pudong area of Shanghai. This figure shows that as the image resolution increases, the fitting accuracy of the SARCoorP-RBFNet model gradually decreases. The reason for this is that as the image resolution increases, the geographic distance represented by a single pixel decreases and brings with it less tolerance for fitting errors. Table 2 indicates that for images with a resolution of 1 m, the SARCoorP-RBFNet model has the largest fitting
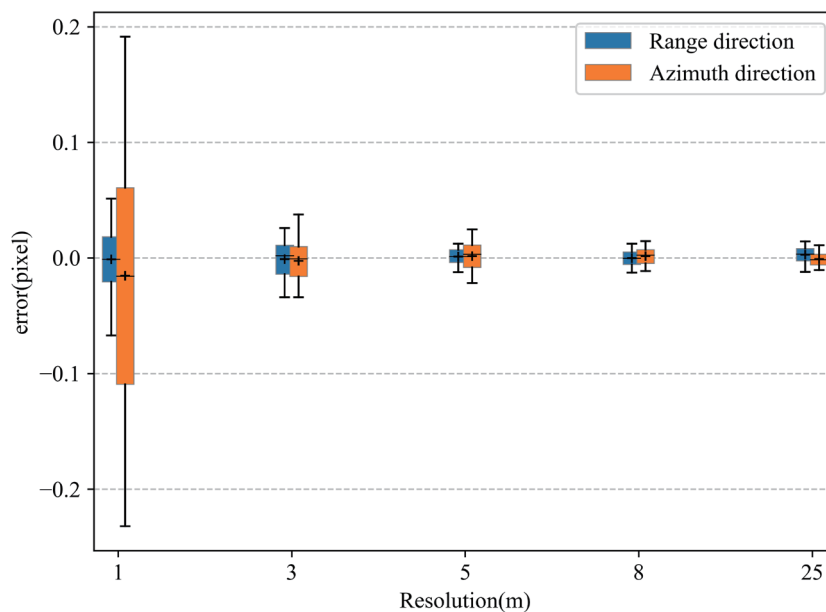

Fig. 4.   (Color online) Distribution of test error findings of each image in Shanghai area.

Table 2
Single image fitting results for five resolutions.

Resolution (m)	Image ID	*RMSE* (pixel)	
		Range direction	Azimuth direction
1	SP_9563	0.02712	0.10448
3	SP_1726	0.01427	0.01862
5	SP_6958	0.00719	0.01255
8	SP_1557	0.00653	0.00694
25	SP_3580	0.00617	0.00603

errors of 0.02712 and 0.10448 pixels in the range and azimuth directions, respectively. For images with a resolution of 25 m, the fitting errors in both directions, which are 0.00617 and 0.00603 pixels, respectively, are the smallest. Although the fitting accuracy of the SARCoorP-RBFNet model decreases with increasing resolution, the lowest accuracy in the distance direction is still within 5% of the pixel range, and thus it can theoretically replace the RD model.

4.2 Analyzing the accuracy of the SARCoorP-RBFNet model in fitting images of different regions at the same resolution

Figure 5 shows the fitting error distribution of the SARCoorP-RBFNet model for a single image of five cities (Pudong, Fangshan, Chengdu, Xingtai, and Nanjing) under the QPSI model.

According to Table 3, the accuracy of the SARCoorP-RBFNet model is less than 0.9% pixel for different areas of the same resolution. The fitting accuracy varies slightly from region to region owing to differences in topography, building density, and environment. The Fangshan area has the highest fitting accuracy in the distance direction (0.00409 pixels), whereas the Chengdu area yielded the highest fitting accuracy in the azimuth direction (0.00585 pixels). Figure 5 shows that the error distribution of images in various places is largely consistent, although there are a few outliers in Xingtai, Hebei Province. Overall, the fitting accuracy is good, which sufficiently demonstrates that the fitting result of the SARCoorP-RBFNet model is consistent and less affected by the topography.
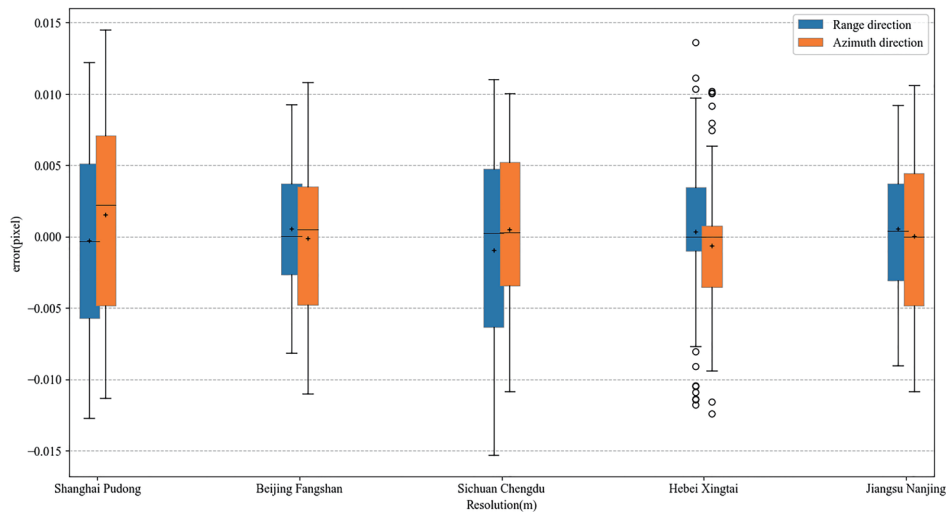

Fig. 5. (Color online) Distribution of fitting results of RBF neural network for five regions under QPSI model.

Table 3
Fitting results for single image of five areas with a resolution of 8 m.

Area	Image ID	RMSE (pixel)	
		Range direction	Azimuth direction
Shanghai Pudong	SP_1557	0.02712	0.10448
Beijing Fangshan	BF_3116	0.01427	0.01862
Sichuan Chengdu	SC_4783	0.00719	0.01255
Hebei Xingtai	HX_4208	0.00653	0.00694
Jiangsu Nanjing	JN_5002	0.00617	0.00603

4.3 Evaluation of fitting accuracy of SARCoorP-RBFNet model trained for multiple images.

4.3.1 Images of various imaging modes in Shanghai region

Figure 6 shows the fitting results of the SARCoorP-RBFNet model under the multi-mode imaging mixed training scenario in the Shanghai area, including the error results of the multi-mode imaging mixed sample image test and the independent sample tests. Additionally, Fig. 6 shows a Shapefile diagram of the distribution location of the images of each imaging mode.

Table 4 shows that the fitting accuracy of the network model obtained using mixed training with multi-scene images in the same area is reduced by two orders of magnitude on average. The error line graph in Fig. 6(a) shows slight variations in the fitting accuracy of the network model under different imaging modes. The Shapefile diagram in Fig. 6(b) indicates overlapping regions between different images, which can result in the reduced fitting accuracy of the network model.

These tests show that when training with a mixture of multi-scene images from the same geographic region, which have different resolutions due to different imaging modalities, resulting in image overlap, there is a significant impact on the fitting accuracy of SARCoorP-RBFNet.
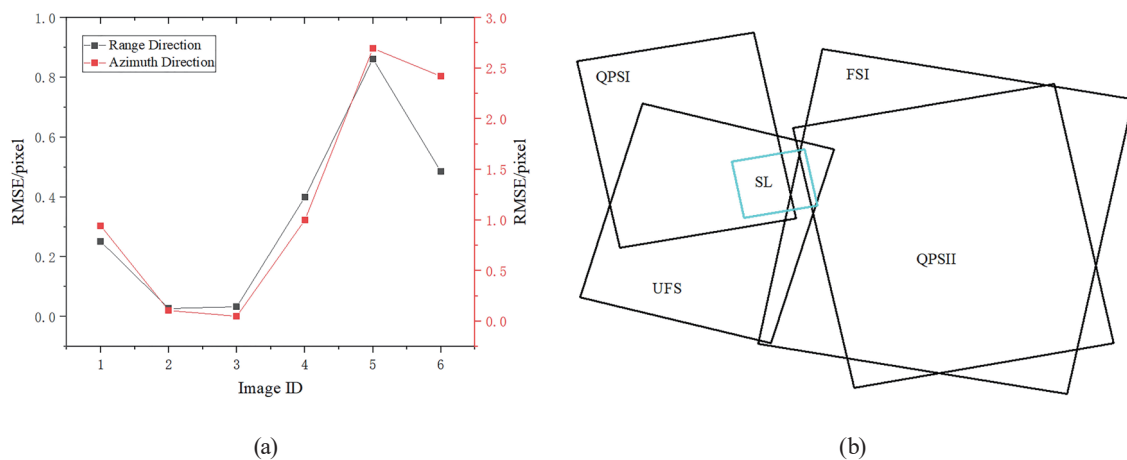

Fig. 6.   (Color online) Results of SARCoorP-RBFNet model fitting (a) and Shapefile image (b). (a) Distribution of fitting error. (b) Shapefile images of various imaging modes.

Table 4
Test results of various imaging modes in Shanghai's Pudong region.

Image model	Image ID	*RMSE* (pixel)	
		Range direction	Azimuth direction
Mixed Sample	1	0.251463	0.942022
SL	2	0.027255	0.105849
UFS	3	0.032625	0.048549
FSI	4	0.399985	0.999629
QPSI	5	0.861758	2.696055
QPSII	6	0.484541	2.418062

4.3.2 National area's image in QPSI imaging mode

Figure 7(a) shows the model fitting errors produced by the mixed training of 16 areas in the QPSI mode, including the results of the mixed sample test error and the results of the single image test error for each region. The Shapefile image distribution by region is shown in Fig. 7(b).

According to the data in Table 5, the fitting accuracy of the network model is similar to that of training on a single scene when different regions of the same imaging mode are mixed-trained, and the fitting accuracy of the distance and azimuth directions is higher than 2% pixels. The distribution of fitting errors for each region is shown in Fig. 7(a), and the error curves of most regions' exhibit little variation. The right side of Fig. 7(b) shows the image distribution of each region, with no overlap between any of the area images. This indicates that even when images from different regions of the same imaging mode are mixed-trained, the proposed method still has high fitting and generalization capabilities.

5. Discussion and Conclusions

To address the demand for the intelligent geometric processing of SAR images, we have innovatively proposed a neural-network-based intelligent fitting model. This model is designed to construct fitting models for single- and even multi-scene SAR imagery in the context of image geometric processing, utilizing SARCoorP-RBFNet for the feature learning of the spatial mapping relationship of SAR image coordinate point pairs. We have demonstrated that our

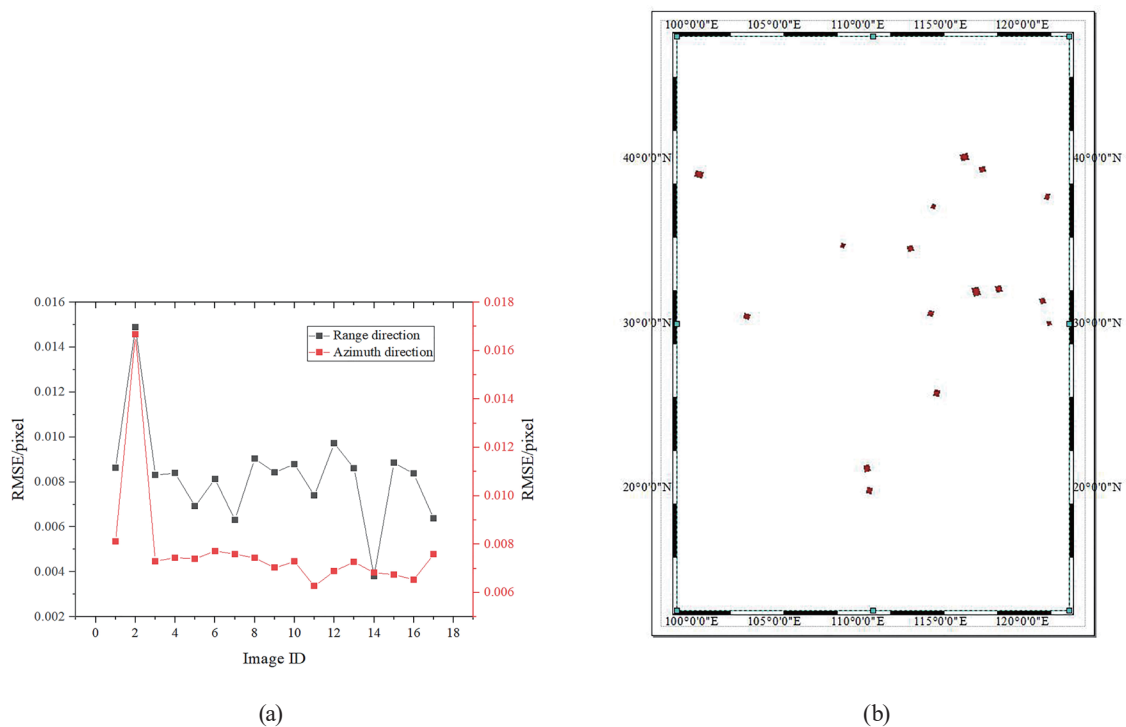(a)   (b)

Fig. 7.   (Color online) Distribution of test results for each image in QPSI mode (a) and Shapefile image (b). (a) Test error maps for each area. (b) Shapefile distribution for each region.

Table 5
Results of testing each image in QPSI model.

Area	Image ID	*RMSE* (pixel)	
		Range direction	Azimuth direction
Mixed Sample	0	0.008630	0.008121
Anhui	1	0.014884	0.016672
Henan	2	0.008315	0.007296
Hebei	3	0.008391	0.007443
Shanghai	4	0.006914	0.007389
Zhejiang	5	0.008138	0.007718
Jiangsu	6	0.006312	0.007592
Shandong	7	0.009039	0.007431
Shanxi	8	0.008423	0.007025
Hainan	9	0.008802	0.007277
Tianjin	10	0.007391	0.006264
Gansu	11	0.009724	0.006887
Jiangxi	12	0.008604	0.007269
Beijing	13	0.003813	0.006820
Sichuang	14	0.008853	0.006746
Hubei	15	0.008370	0.006537
Guangdong	16	0.006366	0.007580

method achieves an accuracy in fitting the RD model that is superior to 5% of pixels, which is deemed effective in practical engineering applications. The following provides a detailed description of our conclusions.

(1) The SARCoorP-RBFNet model exhibits excellent fitting performance on single-scene imagery. However, there are variations in the fitting accuracy of the SAR-CoorP-RBFNet model when applied to different-resolution images of the same area. It performs exceptionally well on low-resolution images such as QPSI, achieving a marked pixel-level fitting accuracy of up to 0.7%. The fitting accuracy of the SAR-CoorP-RBFNet model is slightly lower on high-resolution images (such as SL and UFS) than on low-resolution images. We can control the fitting accuracy in the range of less than 5% of a pixel in the distance direction. For images of the same resolution but different areas, the fitting errors of the SARCoorP-RBFNet model exhibit slight fluctuations in both directions, with a pixel-level fitting accuracy of less than 0.9%. This suggests that the fitting accuracy of this model is minimally affected by terrain factors. Hence, it indicates that terrain factors do not significantly impact the feasibility of replacing the RD model with the SARCoorP-RBFNet model. Therefore, in theory, the SARCoorP-RBFNet model can serve as a viable alternative to the RD model.

(2) The SARCoorP-RBFNet model, based on training with a blend of multiple images, has certain limitations. This model is only suitable for training with mixed samples from different regions. Compared with the models trained on single-scene images, the model's fitting accuracy for different region images is reduced by two orders of magnitude, and the fitting accuracy for the same region images is also diminished. Therefore, when there are significant regional differences in the mixed images, the SARCoorP-RBFNet model, in theory, can still serve as a substitute for the RD model.

These results lay the foundation for establishing the efficient deep-learning-based geometric processing of SAR images. Although this study has achieved certain accomplishments, it still has limitations. The current geometric imaging models face challenges in achieving global image geometric processing. Therefore, future research should focus on developing a deep network fitting model suitable for global images to accomplish their geometric processing.

Acknowledgments

References

1   J. C. Curlander: IEEE Trans. Geosci. Remote Sens. **20** (1982) 359. https://doi.org/10.1109/TGRS.1982.350455
2   G. Zhang, W. Fei, Z. Li, X. Zhu, and X. Tang: Acta Geod. Cartogra. Sin. **39** (2010) 264. https://oversea.cnki.net/kcms/detail/detail.aspx?dbcode=CJFD&filename=CHXB201003011&dbname=CJFD2010
3   S. Nedelcu and B. Brian: Remote Sens. **44** (2018) 191. https://doi.org/10.1080/07038992.2018.1479635
4   T. Y. Wang, G. Zhang, L. Yu, R. S. Zhao, M. J. Deng, and K. Xu: Sensors **17** (2017) 2005. https://doi.org/10.3390/s17092005
5   G. Zhang, W. Fei, Z. Li, X. Zhu, and D. Li: Photogramm. Eng. Remote Sens. **6** (2010) 727. https://doi.org/10.14358/PERS.76.6.727
6   W. Huang, G. Zhang, and D. Li: IEEE Trans. Geosci. Remote Sens. **54** (2016) 4355. https://doi.org/10.1109/TGRS.2016.2541144
7   X. Zhu, S. Montazeri, M. Ali, Y. Hua, Y. Wang, L. Mou, Y. Shi, F. Xu, and R. Bamler: IEEE Geosci. Remote Sens Mag. **9** (2021) 143. https://doi.org/10.1109/MGRS.2020.3046356
8   J. Pan, Y. Zi, J. Chen, Z. Zhou, and B. Wang: IEEE Trans. Ind. Electron. **65** (2018) 4973. https://doi.org/10.1109/TIE.2017.2767540
9   K. Saitulasi and N. Deepa: 2021 Int. Conf. Comput. Commun. Inf. (ICCCI, 2021) 1–3. https://doi.org/10.1109/ICCCI50826.2021.9456999
10   W. E. Brown: Amer. Geophys. Uni. Spr. Meet. (1981) 25.
11   R. Bamler and B. Schättler: SAR geocoding: data and systems (Wichmann, Karlsruhe, 1993).
12   D. Vassilaki and C. Ioannidis: Proc. 30th EARSeL Symp.: Remote Sens. for Sci. Educ. Cult. (2010) 573.
13   A. Eftekhari, M. Saadatseresht, and M. Motagh: Sensors **13** (2013) 12030. https://doi.org/10.3390/s130912030
14   P. Capaldo, M. Crespi, L. D. Vendictis, and F. Fratarcangeli: 30th Annu. EARSeL Symp. Remote Sens. Sci., Edu., Nat. Cult. Heritage (EARSeL 2010) 483–490.
15   K. S. S. Sekhar, A. S. Kumar, and V. K. Dadhwal: Int J. Remote Sens. **35** (2014) 7303. https://doi.org/10.1080/01431161.2014.968266
16   H. Furukawa: arXiv **117** (2017) 13. https://doi.org/10.48550/arXiv.1708.07920
17   E. Mason, B. Yonel, and B. Yazici: Proc. Synth. Aperture Radar Imagery XXIV (SPIE, 2017) 1020104. https://doi.org/10.1117/12.2267831
18   N. Anantrasirichai, J. Biggs, F. Albino, and D. Bull: Remote Sens. Environ. **230** (2019) 111179. https://doi.org/10.1016/j.rse.2019.04.032
19   S. Valade, A. Ley, F. Massimetti, O. D'hondt, M. Laiolo, D. Coppola, D. Loibl, O. Hellwich, and T. R. Walter: Remote Sens. **11** (2019) 1528. https://doi.org/10.3390/rs11131528
20   M. E. Gaddes, A. Hooper, M. Bagnardi, H. Inman, and F. Albino: J. Geophys. Res.: Solid Earth **123** (2018) 10. https://doi.org/10.1029/2018JB016210
21   M. Gaddes, A. Hooper, and F. Albino: EarthArXiv. (2021). https://doi.org/10.31223/X5CW2J
22   M. Reichstein, G. Camps-Valls, B. Stevens, M. Jung, J. Denzler, N. Carvalhais, and Prabhat: Nature **566** (2019) 195. https://doi.org/10.1038/s41586-019-0912-1
23   G. Zhang, Q. Qiang, Y. Luo, Y. Zhu, H. Gu, and X. Zhu: Photogramm. Rec. **27** (2012) 94. https://doi.org/10.1111/j.1477-9730.2011.00667.x

24 J. Chen, Q. Zeng, J. Jian, F. Ye, and L. Zhu: Acta. Geod. Cartogra. Sin. **45** (2016) 1434. https://doi.org/10.11947/j.AGCS.2016.20160182

25 G. Zhang, M. Deng, C. Cai, and R. Zhao: Senors **19** (2019) 2367. https://doi.org/10.3390/s19102367

26 T. Ding and H. Zhou: J. Harbin. Inst. Technol. **37** (2005) 272. https://www.researchgate.net/publication/287534768_Prediction_method_research_based_on_radial_basis_function_neural_network

27 M. Li, B. Verma: Expert Syst. Appl. **45** (2016) 161. https://doi.org/10.1016/j.eswa.2015.09.033

28 A. Tatar, A. Barati, A. Najafi, and A. Mohammadi: Pet. Sci. Technol. **37** (2019) 1306. https://doi.org/10.1080/10916466.2019.1575878